

Mobile Vehicle-Mounted Mid-Infrared Dual-Comb Spectrometer for Outdoor Trace Gas Detection

XUTIAN JING^{1,†}, KAIWEN WEI^{1,†}, XIONG QIN¹, JUNWEI LI¹, XINGYIN YANG¹,
ZHAOTING HUANG¹, JIANPING ZHANG¹, CHENHAO SUN¹, CHENYU LIU¹,
ZEJIANG DENG¹, ZHIWEI ZHU¹, DAPING LUO¹, CHENGLIN GU^{1,2}, AND WENXUE LI^{1,3}

¹State Key Laboratory of Precision Spectroscopy, East China Normal University, Shanghai 200062, China

²e-mail: clgu@lps.ecnu.edu.cn

³e-mail: wxli@phy.ecnu.edu.cn

[†]These authors contributed equally to this work

Received XX Month XXXX; revised XX Month, XXXX; accepted XX Month XXXX; posted XX Month XXXX (Doc. ID XXXXX);
published XX Month XXXX

Advances in mid-infrared (MIR) dual-comb spectroscopy (DCS) have greatly boosted molecular detection in recent years. The ability of DCS to precisely identify and quantify outdoor atmospheric trace gases makes it attractive for applications in agriculture, energy, and industrial monitoring. Here, we demonstrate a vehicle-mounted MIR DCS system based on optical-optical modulated frequency combs (OMFCs), which achieve passive mutual coherence between the two combs. The system enables point-by-point and drive-by measurements under various outdoor conditions, achieving minimum detection limits of 45 parts per billion (ppb) for methane (CH₄) and 46 parts per million (ppm) for water vapor (H₂O) at 100-s averaging time. Finally, we mapped the two-dimensional concentration field and the concentration probability distribution near a CH₄ source, and compared them with the contemporaneous wind rose. These experiments demonstrate the system's capability for localized gas identification and in situ quantification with high temporal and spatial resolution.

I. INTRODUCTION

As a tool for precise time-frequency measurement, optical frequency comb technology demonstrated its powerful strengths in many areas as soon as it was developed [1–4]. DCS combines broadband coverage, high frequency accuracy, and rapid acquisition by mapping optical frequencies into the radio-frequency domain through two combs with slightly detuned repetition rates [5]. Operating in the MIR, where many molecules exhibit intense fundamental-band absorptions, DCS provides strong sensitivity and high precision even with relatively short optical paths [6,7]. These characteristics make MIR-DCS highly promising for outdoor gas sensing across environmental, agricultural, and energy-related applications [8–11].

In recent years, pioneering efforts, particularly those led by National Institute of Standards and Technology (NIST) and collaborators, have sought to transfer DCS from the laboratory to outdoor environments. A series of representative studies—such as the first outdoor NIR DCS [12], unmanned aerial vehicle (UAV)-assisted DCS [13], multi-reflector open-path configuration for wide-area monitoring [14], the first MIR DCS field test [15], and a broadband open-path system extending into the 4.5–5 μm region for simultaneous multispecies detection [16]—have demonstrated that field-deployable

DCS has progressively evolved to deliver increasingly broad practical utility in outdoor sensing. These demonstrations typically relied on a telescope–retroreflector pair to form a long open path for integrated absorption measurements, retrieving path-averaged gas concentrations. While this configuration is highly effective for regional monitoring and flux estimation, certain scenarios—such as constrained underground tunnels, airborne or high-altitude platforms, and planetary rover missions—often require localized gas identification and quantification [17–20]. Although a number of point sensors, such as tunable diode laser absorption spectroscopy, cavity ring-down spectroscopy, and portable Fourier-transform spectrometers, can provide localized measurements, each technique faces inherent trade-offs [21–24]. In contrast, DCS uniquely combines broad spectral coverage, high spectral resolution, rapid acquisition, and intrinsic frequency accuracy without external calibration, making it a powerful approach for point-resolved measurements in complex field environments. Although substantial progress has been made, most existing DCS platforms still rely on laboratory-grade stabilization electronics and pulse-shaping modules, which limit their portability in dynamic outdoor scenarios. As a result, translating DCS into a truly mobile platform remains particularly challenging [25]. This motivates the development of a mobile-scanning DCS system capable of robust operation in field conditions.

In this study, we developed a vehicle-mounted MIR DCS system operating near $3.4\ \mu\text{m}$ for outdoor trace-gas detection and in situ measurements. Two key design strategies enable robust field performance: the use of optical–optical modulation to passively maintain mutual coherence between the two frequency combs [26,27], and the implementation of all polarization-maintaining figure-9 oscillators that provide exceptional mechanical stability for mobile operation [28,29]. Together, these features allow the system to maintain long-term stability under outdoor conditions. The DCS achieved a figure of merit of $3.4 \times 10^6\ \sqrt{\text{Hz}}$, indicating a high overall sensitivity-to-bandwidth performance. Field tests were conducted across multiple scenarios, including both point-by-point measurements and drive-by scanning. Furthermore, a simulated natural-gas leakage experiment enabled spatial and temporal mapping of CH_4 and H_2O concentrations. To quantify mobile performance, we define a noise-equivalent concentration gradient (NECG), which links the Allan deviation to the distance traveled during averaging. At a driving speed of $2\ \text{m/s}$, the system resolves CH_4 changes of $\sim 200\ \text{ppb}$ over $2\ \text{m}$ and $\sim 25\ \text{ppb}$ over $200\ \text{m}$, corresponding to NECG values on the order of $100\ \text{ppb/m}$ and $0.1\ \text{ppb/m}$. This illustrates the system’s capability to detect both sharp local plumes and weak large-scale gradients during vehicle-based scanning. These results demonstrate that the proposed vehicle-mounted DCS system functions effectively as a mobile laboratory capable of performing in situ measurements across diverse outdoor environments.

II. Dual-comb spectrometer field deployment

A. Dual-comb spectrometer

The MIR dual-comb spectrometer is built upon an optical–optical modulation technique, which enables passive mutual coherence between the two combs [26,27,30]. The entire system is compactly integrated, thermally insulated, and vibration-isolated to withstand outdoor environmental conditions. The overall size of the DCS unit is $28 \times 30 \times 25\ \text{cm}^3$ ($L \times W \times H$), corresponding to a total volume of about $21\ \text{L}$ and a total weight of approximately $22\ \text{kg}$. Together with the gas cell and photodetector, the whole setup is mounted on a $30 \times 60\ \text{cm}$ optical breadboard. Each optical module is connected through fiber flanges and collimator interfaces, allowing convenient plug-and-play operation. The typical power consumption is approximately $20\ \text{W}$, enabling long-term continuous operation using a portable outdoor power supply.

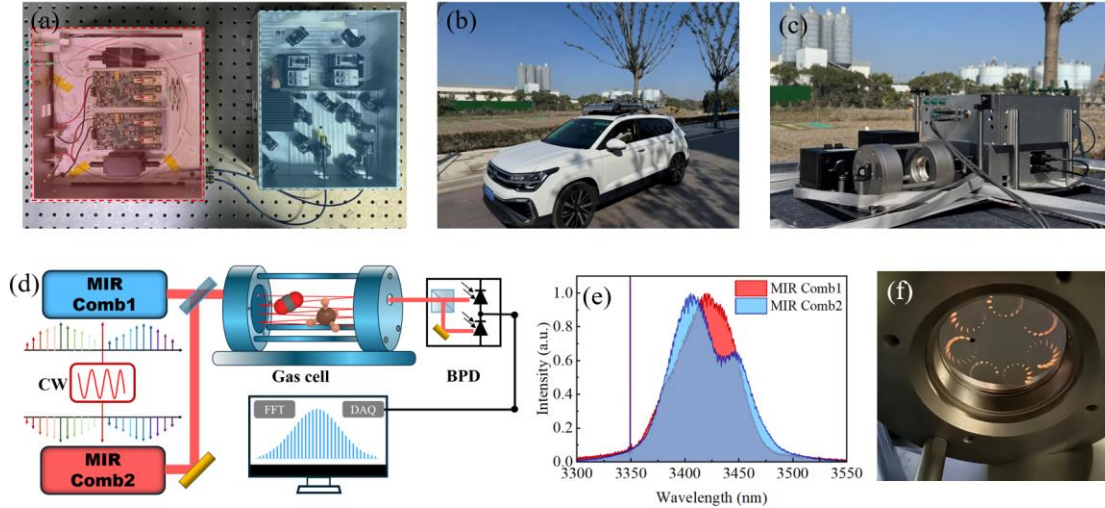


Fig. 1. Overview of the integrated MIR dual-comb spectrometer. (a) Photograph of the MIR DCS system. The red-shaded area contains two compact nonlinear amplifying loop mirror mode-locked fiber lasers and their amplifiers, while the blue-shaded area represents the free-space optical path for optical parametric amplification (OPA). The two modules are connected via fiber collimators. (b) Illustration of the vehicle-based field deployment during outdoor measurements. (c) Vehicle-mounted configuration showing the DCS and open gas cell installed on the SUV roof, fully exposed to ambient air. (d) Schematic of the optical-optical modulated dual-comb principle, where two mid-infrared combs share a common CW reference laser to achieve passive mutual coherence. (e) Output MIR spectra of the two OPA branches. (f) Beam spots observed on one side of the Herriott gas cell.

Each comb oscillator employs an all polarization-maintaining Yb-doped fiber figure-9 laser operating at a repetition rate of 56.5 MHz, featuring excellent vibration immunity and low noise, as shown in Fig. 1(a). A subsequent single-stage fiber amplifier delivers up to 550 mW average power with ~ 4 ps pulse duration centered at 1030 nm. In the free-space nonlinear conversion stage, the two MIR combs are passively referenced to a common CW laser centered at 3.35 μm , as illustrated in Fig. 1(d), ensuring both combs inherit the CW frequency f_{cw} stability while greatly simplifying the system complexity. The combined MIR dual-comb beam, with a total output power of 5 mW, is coupled into an open Herriott multi-pass gas cell with a total optical path length of 25 m, thereby enhancing detection sensitivity through extended light-molecule interaction. The heterodyne signal is detected by a balanced photodetector (Vigo, PVI-4TE-5), with the repetition-rate difference set to approximately 400 Hz for rapid dual-comb acquisition. The balanced configuration effectively suppresses common-mode intensity noise and residual etalons, improving the per-tooth signal-to-noise ratio (SNR) by 14 dB compared with single-ended detection (Vigo, PVI-4TE-3.4). The detected interferogram is digitized by a 12-bit acquisition card (AlazarTech, ATS9350) for further FFT-based spectral retrieval.

B. Measurement procedure

The vehicle-mounted field experiments were carried out in two parts. First, a series of point-by-point measurements were performed at seven representative locations within the Minhang campus of East China Normal University (ECNU), followed by drive-by scanning measurements along a riverside road to evaluate the spatial response of the system, as shown in Fig. 2 (b). On the same day, a long-distance stability test was conducted by driving the vehicle from ECNU (Minhang District) to the Laogang Solid Waste Treatment Center (Pudong District), covering a total distance of 47 km, as shown in Fig. 2 (a).

During the measurements, the weather was partly cloudy with occasional light gusts (around 2 m/s), and the ambient temperature varied between 28 °C and 33 °C. The average driving speed was approximately 40 km/h, with road conditions including both urban streets and expressways, where the instantaneous speed occasionally reached 100 km/h. The baseline spectral stability, evaluated from the relative standard deviation of a normalized line-free region, was 2.6%.

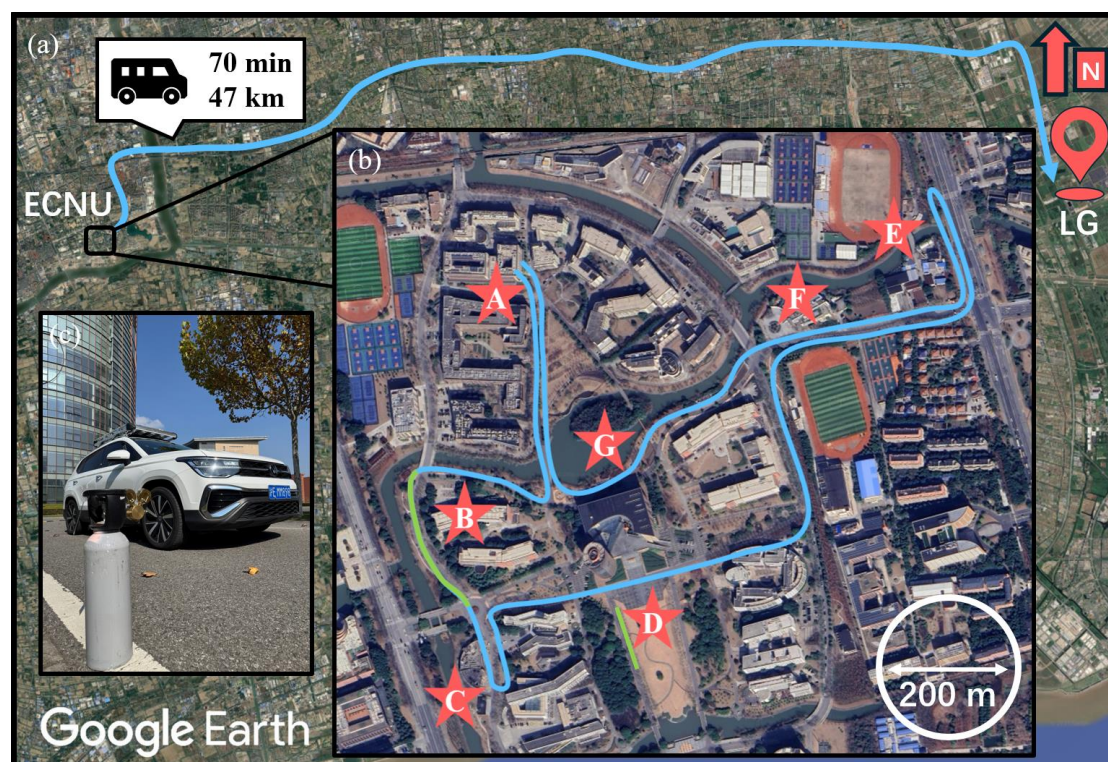


Fig. 2. Overview of the field deployment experiment. (a) Map of ECNU and the surrounding urban area of Shanghai. The blue trace shows the 47 km driving route from ECNU to Laogang Town, completed in approximately 70 min. (b) Route map of the on-campus field test. Locations A–G correspond to the Optics Building, Teaching Building, Cafeteria I, Library, Waste Compression Station, Cafeteria II, and Lakeside, respectively. The measurement started from point A and followed a counterclockwise route. A 200 m mobile continuous measurement was performed near point B (green segment), while a simulated natural-gas leakage inspection was conducted near point D (green segment). (c) On site test photos simulating natural-gas leakage. Background map data from Google Earth.

After validating the system’s performance in ambient atmospheric measurements, further experiments were conducted to assess its capability for detecting localized gas emissions. In outdoor scenarios such as energy facilities and industrial sites, gas leaks often occur as spatially confined plumes with strong concentration gradients, where path-integrated open-path DCS configurations may fail to provide spatially resolved information [31]. To evaluate the system’s performance under such conditions, a simulated natural-gas (with ~95% CH₄ content) leakage experiment was carried out under controlled outdoor environments to investigate the system’s spatial and temporal response to localized CH₄ plumes.

The leakage experiment was conducted on a quiet campus road, as shown the green segment near location D in Fig. 2(b), where two standard natural-gas cylinders (with ~95% CH₄ content) were placed approximately 30 m apart. The controlled release rates were set to 1.0 g/min and 1.2 g/min, respectively,

with each nozzle positioned about 0.5 m above the ground. The cylinders were located at a perpendicular distance of ~ 3 m from the driving path of the vehicle. During the measurements, ambient wind was nearly calm, allowing the spatial diffusion of CH_4 to be approximated as isotropic, which ensured that the expanding plume intersected the open Herriott gas cell optical path. The DCS-equipped vehicle was then driven slowly along the road at a speed of approximately 5 km/h, covering a distance of about 100 m, while continuously recording dual-comb spectra throughout the entire process. During the experiment, no pedestrians were present, and the optical source was carefully shielded to prevent stray-light leakage.

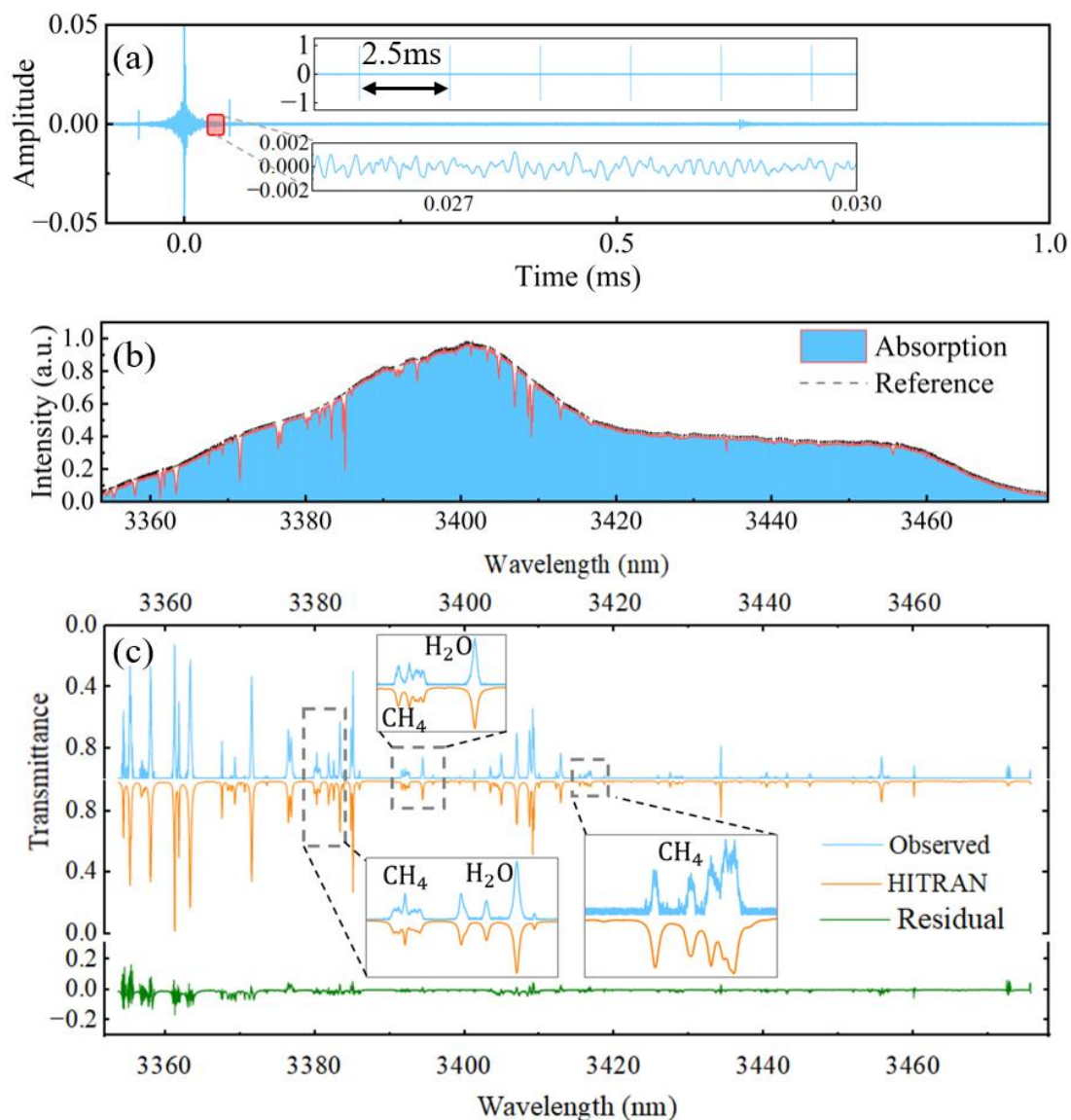


Fig. 3. Dual-comb spectroscopy of CH_4 and H_2O . (a) In the time domain, the multi-heterodyne signal from two MIR frequency combs results in a periodic interferogram with a recurrence period of $1/\Delta f_r = 2.5$ ms. A sequence of 6 interferograms is shown in the inset (top). The free-induction decay signature of molecular absorption is shown in the bottom inset, highlighting the high temporal resolution of a complete absorption cycle. (b) Outdoor vehicle-based dual-comb absorption spectrum (red line) of ambient CH_4 and H_2O , averaged 10 s, together with the fitted background reference spectrum (dashed black line). (c) The retrieved transmittance spectrum (blue line) is compared with the simulated HITRAN spectrum (orange line), and the residuals are plotted in green. The inset highlights a zoomed-in spectral region, showing excellent agreement between the measured and simulated spectra.

III. Results and Discussion

The outdoor environment is inherently dynamic, yet the developed DCS system maintains high stability during field operation [25]. Although the repetition rates of free-running fiber lasers can, in principle, vary with temperature-induced changes in the fiber-cavity optical length, the thermally insulated mechanical design effectively suppresses such effects. For a 3.65-m fused-silica cavity, the combined thermal expansion and thermo-optic coefficients correspond to an estimated $df_r/dT \approx -400\text{Hz/K}$ [32,33]. In practice, however, once thermal equilibrium is reached outdoors, the measured f_r drift remains below 5 Hz over 10 minutes. In the optical-optical modulated DCS configuration, f_r variations manifest as spectral scaling, whereas CW laser drift causes a global frequency shift. Field measurements show that the CW laser drifted by less than 40 MHz within 10 minutes, with a standard deviation of 5.9 MHz, confirming excellent frequency stability under ambient outdoor conditions. Since the impact of f_{cw} drift on the spectrum is far smaller than that caused by fluctuations in the Δf_r between the two combs, the f_{cw} is treated as effectively constant. An automated algorithm adjusts the Δf_r such that the measured absorption features remain strictly aligned with HITRAN data [34], thereby removing repetition-rate-induced spectral distortions at the algorithmic level.

Table 1. Measured CH₄ and H₂O concentrations at seven representative locations within the ECNU campus. The concentrations were retrieved by comparing the measured transmission spectra with HITRAN-based reference spectra using a least-squares fitting method.

Mole Fraction	A	B	C	D	E	F	G
CH ₄ (ppm)	1.98	1.69	1.78	1.74	1.65	1.74	1.87
H ₂ O (ppm)	20760	28860	25430	25880	26710	26080	27090

*Considering the noise-limited concentration sensitivity, the CH₄ and H₂O mole fractions should be interpreted within ranges of $c(\text{CH}_4) \pm 75$ ppb and $c(\text{H}_2\text{O}) \pm 76$ ppm, respectively.

To evaluate the detection sensitivity of the dual-comb spectrometer prior to the field deployment, the system was operated continuously for 2000 s in an open area with well-mixed air, recording one interferogram per second. From Fig. 3(c), small discrepancies between the measured transmittance and the HITRAN spectrum can be observed. To quantify the noise level, we selected a line-free spectral region from 3386.5 to 3391.5 nm, where the ideal transmission is $T = 1$, and computed the RMS error of the measured transmittance. For a 10-s averaged spectrum, the RMS error in this absorption-free region is 0.33%. For atmospheric CH₄ at a mole fraction of 1.9 ppm and a 25-m optical path, the representative CH₄ absorption feature at 3379.9 nm exhibits an absorbance of $\alpha = 0.0834$. Considering the noise-limited minimum observable transmission change [35], this corresponds to a concentration sensitivity of approximately 75 ppb (or 1875ppb-m). For H₂O at a 1% mole fraction, the H₂O line at 3371.5 nm ($\alpha = 0.4308$) yields a corresponding sensitivity of ~ 76 ppm under the same conditions.

Fig. 4(c) and 4(d) summarize the SNR behavior within a 1000-s acquisition window and the corresponding Allan deviations of the retrieved CH₄ and H₂O concentrations. The average spectral SNR increases proportionally to the square root of the averaging time τ , indicating that the measurement performance is predominantly limited by white noise. The fitted slope on the log-log scale closely follows the theoretical $\sqrt{\tau}$ dependence, confirming the absence of significant correlated noise sources within the investigated time range. The Allan deviation of gas concentration provides a quantitative measure of the temporal stability of the DCS retrieval. For both CH₄ and H₂O, the Allan deviation

decreases with averaging time at short τ , reaching minimum values at approximately 150 s and 300 s, respectively, before increasing at longer averaging times. Analysis of the raw spectra reveals that, when the averaging time exceeds roughly 200 s, noticeable spectral-axis misalignment emerges among successive measurements. Although our wavelength-calibration algorithm effectively suppresses distortions induced by repetition-rate fluctuations of the two free-running oscillators, the residual frequency drift of the f_{cw} reference laser begins to dominate over long time intervals. This drift causes gradual horizontal shifts of the spectra, blurring absorption features—particularly the sharper H₂O lines—and ultimately leading to the observed rise in Allan deviation at long averaging times.

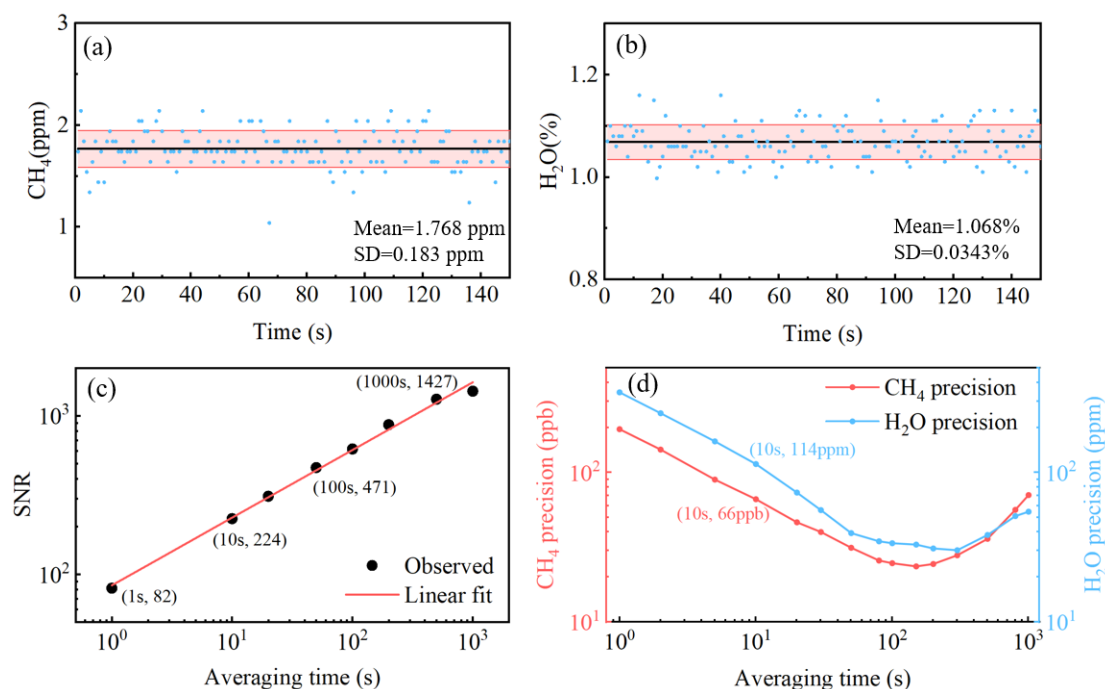


Fig. 4. Background concentrations of (a) CH₄ and (b) H₂O measured by the vehicle-mounted DCS system during a 200-m roadside scan. (c) SNR of the retrieved spectra as a function of averaging time. The SNR follows a $\sqrt{\tau}$ dependence, as confirmed by the linear fit in the log–log plot. (d) Allan deviation analysis of CH₄ and H₂O concentrations, showing precision limits of 66 ppb for CH₄ and 114 ppm for H₂O at 10 s averaging time.

Table 1. summarizes the CH₄ and H₂O mole fractions measured at seven representative locations across the ECNU campus, as marked in Fig. 2(b). Each data point was retrieved from a 10-s average of the dual-comb interferograms. The measured CH₄ concentrations range from 1.65 ppm to 1.98 ppm, yielding a mean value of 1.78 ppm and a standard deviation of 110 ppb. This deviation is larger than the Allan-limited precision of 66 ppb at 10-s averaging, indicating that the fluctuations are influenced not only by instrumental noise but also by small but real spatial variations in ambient CH₄ abundance along the campus environment. In comparison, the measured H₂O concentrations span from 25,430 ppm to 28,860 ppm, with a mean value of 26,730 ppm and a standard deviation of 1,126 ppm. This variation exceeds the corresponding Allan-limited precision of 114 ppm by an order of magnitude, confirming that the system clearly resolves genuine spatial changes in atmospheric humidity. These results demonstrate that the DCS retrieval algorithm maintains high accuracy outdoors and is sensitive enough to distinguish environmental variability from instrumental noise. Fig. 4(a) and 4(b) present the atmospheric background CH₄ and H₂O concentrations measured along the 200-m green trajectory near point B in Fig. 2(b). The

retrieval was performed at a temporal resolution of 1 s, corresponding to a spatial resolution of approximately 1.4 m for a driving speed of 5 km/h. Over this scan, the mean CH₄ concentration is 1.768 ppm with a standard deviation of 0.183 ppm, while the mean H₂O concentration is 1.068% with a standard deviation of 0.0343%. The relatively small fluctuations observed over the entire 200-m path demonstrate that the vehicle-mounted DCS system is capable of performing both point-by-point and drive-by field measurements with sufficient precision and stability for real-world atmospheric monitoring.

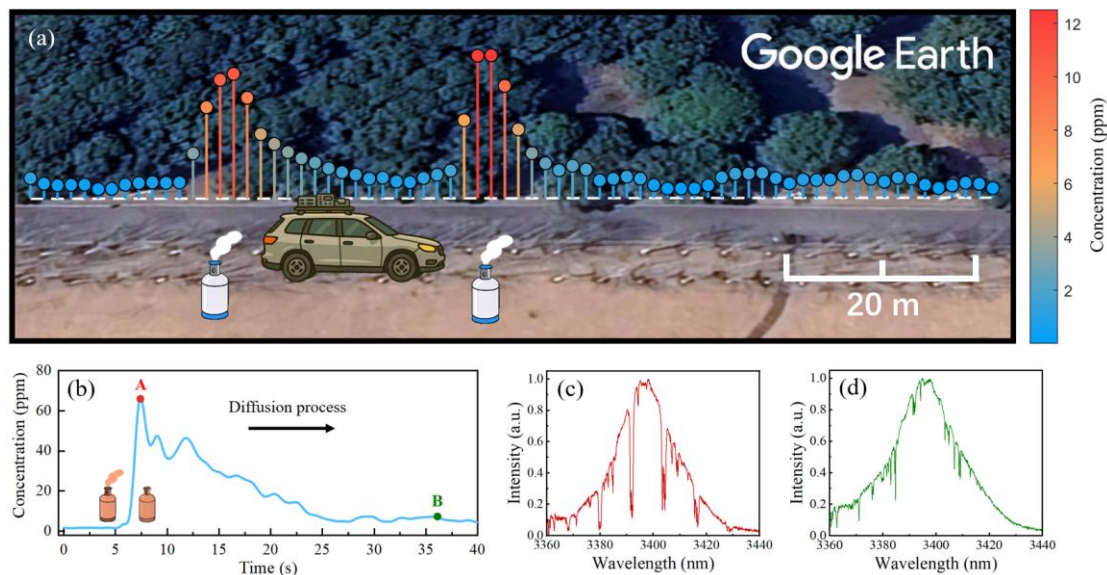


Fig. 5. Simulated natural-gas leakage experiment showing spatial and temporal CH₄ distributions. (a) Spatial mapping of CH₄ concentration obtained by the vehicle-mounted MIR dual-comb spectrometer during roadside inspection of two leakage sources. (b) Time-resolved concentration trace during the controlled on–off release sequence of the gas cylinders, capturing the diffusion process of the CH₄ plume. (c, d) Recorded absorption spectra at moments A and B in (b). Background map data from Google Earth.

Building on these results, a controlled outdoor experiment was further conducted to simulate localized natural-gas leakage, aiming to evaluate the system’s response to transient and spatially confined gas plumes. Fig. 5 summarizes the results of the simulated natural-gas leakage experiment and demonstrates both the spatial-mapping and temporal-tracking capabilities of the vehicle-mounted MIR DCS system. In Fig. 5(a), the reconstructed spatial concentration map clearly reveals two distinct CH₄ plumes originating from the two release points. The plume intensity gradually decays with distance from each cylinder, forming an approximately elliptical distribution shaped by weak ambient air motion. Despite the relatively small release rate, the DCS system successfully captured concentration enhancements exceeding several ppm above the background within a few meters of the leakage sources, demonstrating its high sensitivity and spatial resolution. The temporal evolution of CH₄ concentration during the on–off controlled release sequence is shown in Fig. 5(b). Each activation of the gas nozzle results in a rapid concentration rise, followed by a gradual decay once the release is stopped. The reproducible transient features confirm the system’s ability to track rapid concentration changes with a response time determined by the dual-comb acquisition rate (400 Hz) and the averaging time applied during retrieval. Representative absorption spectra extracted at moments A and B in Fig. 5(b) are displayed in Fig. 5(c) and 5(d). Compared with background spectra, the CH₄ absorption depth increases significantly during plume intersection, while the H₂O features remain nearly unchanged, confirming that the retrieved

variations originate primarily from CH₄. The excellent agreement between the measured spectra and the fitted reference spectra verifies the accuracy of the concentration retrieval even under high-gradient and dynamic outdoor conditions. These results collectively demonstrate that the developed DCS system can reliably identify, quantify, and temporally resolve CH₄ plumes from localized leakage sources, fulfilling key requirements for practical field inspection tasks in energy-safety and industrial-monitoring applications.

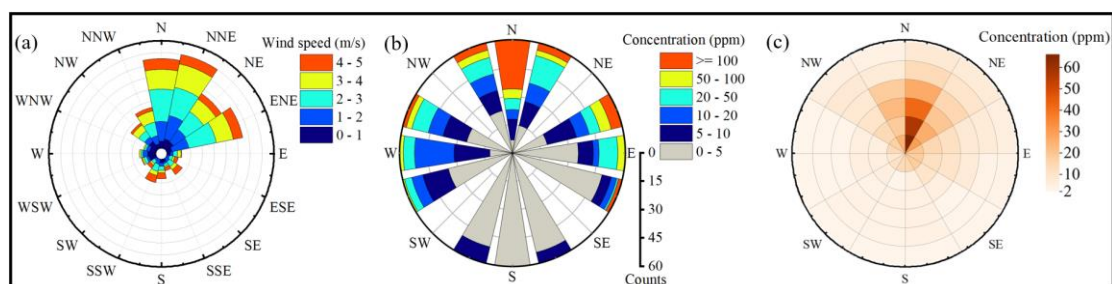


Fig. 6. (a) Wind rose showing the wind direction and speed distribution. (b) CH₄ concentration rose diagram showing the probability distribution across six concentration intervals. (c) Two-dimensional spatial concentration field map with 1 m radial resolution.

The spatial mapping results further validate the system's capability for quantitative plume characterization and its consistency with ambient meteorological conditions. Fig. 6 displays the spatial distribution of CH₄ concentration around a simulated leakage source and the corresponding wind conditions. In Fig. 6(b), a concentration rose diagram is constructed by dividing each angular sector into six discrete ranges (0–5, 5–10, 10–20, 20–50, 50–100, >100 ppm). Each angular direction was measured for 60 s, during which the time-varying concentration data were used to derive the probability distribution of occurrence within different concentration intervals, where the radial length of each colored segment corresponds to the probability in that interval rather than a single averaged value. The pronounced anisotropy observed toward the northeast direction indicates the preferential plume dispersion driven by the prevailing wind, just as shown in Fig. 6(a). It should be noted that at an effective optical interaction length of 25 m, the absorption spectrum of CH₄ tends to reach saturation when the concentration approaches ~100 ppm in this spectral region. Therefore, for measurements involving higher CH₄ concentrations, a gas cell with a shorter optical path length would be required to maintain quantitative accuracy. Fig. 6(c) presents a two-dimensional spatial concentration field map reconstructed with 1 m radial resolution, which clearly visualizes the downwind diffusion pattern consistent with the rose diagrams in Fig. 6(a-b). The consistency among these three visualizations demonstrates the reliability of the vehicle-mounted MIR DCS system in capturing fine spatial variations of CH₄ plumes under outdoor conditions. These results confirm that the system achieves sufficient detection sensitivity and spatial resolution for practical field-deployable CH₄ monitoring. Moreover, this work represents a preliminary step toward the future miniaturization and airborne deployment of the system on UAVs, enabling three-dimensional mapping of atmospheric plumes and validation of atmospheric dispersion models.

In summary, we have demonstrated a compact, vehicle-mounted MIR dual-comb spectrometer for outdoor trace-gas detection. By employing an optical–optical modulated architecture together with all polarization-maintaining figure-9 oscillators, the system reduces complexity while maintaining high stability and sensitivity. Laboratory characterizations confirm sufficient frequency stability of both the f_{CW} and Δf_r , and an adaptive spectral-correction algorithm based on HITRAN H₂O absorption lines effectively mitigates long-term spectral distortions. Field tests across diverse environments, including

urban and campus settings, verified the robustness of the system during extended vehicle operation over a 47-km route. In addition, outdoor simulations of natural-gas leakage demonstrated the capability to capture transient release events in fixed-point mode and to resolve multiple emission sources in drive-by surveys. The system achieved a minimum detection limit of 45 ppb at an optimal averaging time of ~100 s, highlighting its suitability for real-world CH₄ monitoring. Such mobility-enabled DCS systems hold significant potential for scenarios requiring localized concentration measurements, such as unauthorized hazardous-emission sites or clandestine production areas involving narcotics or explosives. The platform can be further adapted for deployment on UAVs, enabling a broader range of applications including high-altitude plume detection, maritime inspection of illegal emissions from cargo vessels, and even atmospheric analysis on planetary rover missions. The optical beams remain confined within the open multi-pass gas cell, eliminating beam escape and ensuring intrinsic eye safety in densely populated environments [36]. Future work will focus on extending the spectral coverage and integrating the system with UAV platforms to enable multispecies detection and expand its applicability across diverse field environments.

References

1. T. W. Hänsch, "Nobel Lecture: Passion for precision," *Rev. Mod. Phys.* **78**(4), 1297–1309 (2006).
2. A. Schliesser, N. Picqué, and T. W. Hänsch, "Mid-infrared frequency combs," *Nature Photon* **6**(7), 440–449 (2012).
3. T. Fortier and E. Baumann, "20 years of developments in optical frequency comb technology and applications," *Commun Phys* **2**(1), 153 (2019).
4. S. A. Diddams, K. Vahala, and T. Udem, "Optical frequency combs: Coherently uniting the electromagnetic spectrum," *Science* **369**(6501), eaay3676 (2020).
5. I. Coddington, N. Newbury, and W. Swann, "Dual-comb spectroscopy," *Optica* **3**(4), 414 (2016).
6. G. Ycas, F. R. Giorgetta, E. Baumann, et al., "High-coherence mid-infrared dual-comb spectroscopy spanning 2.6 to 5.2 μm ," *Nature Photon* **12**(4), 202–208 (2018).
7. A. V. Muraviev, V. O. Smolski, Z. E. Loparo, et al., "Massively parallel sensing of trace molecules and their isotopologues with broadband subharmonic mid-infrared frequency combs," *Nature Photon* **12**(4), 209–214 (2018).
8. N. Kille, R. Chiu, M. Frey, et al., "Separation of Methane Emissions From Agricultural and Natural Gas Sources in the Colorado Front Range," *Geophysical Research Letters* **46**(7), 3990–3998 (2019).
9. C. B. Alden, S. C. Coburn, R. J. Wright, et al., "Single-Blind Quantification of Natural Gas Leaks from 1 km Distance Using Frequency Combs," *Environ. Sci. Technol.* **53**(5), 2908–2917 (2019).
10. D. I. Herman, C. Weerasekara, L. C. Hutcherson, et al., "Precise multispecies agricultural gas flux determined using broadband open-path dual-comb spectroscopy," *Sci. Adv.* **7**(14), eabe9765 (2021).
11. G. J. Mead, D. I. Herman, F. R. Giorgetta, et al., "Apportionment and Inventory Optimization of Agriculture and Energy Sector Methane Emissions Using Multi-Month Trace Gas Measurements in Northern Colorado," *Geophysical Research Letters* **51**(2), e2023GL105973 (2024).
12. G. B. Rieker, F. R. Giorgetta, W. C. Swann, et al., "Frequency-comb-based remote sensing of greenhouse gases over kilometer air paths," *Optica* **1**(5), 290 (2014).
13. K. C. Cossel, E. M. Waxman, F. R. Giorgetta, et al., "Open-path dual-comb spectroscopy to an airborne retroreflector," *Optica* **4**(7), 724 (2017).
14. S. Coburn, C. B. Alden, R. Wright, et al., "Regional trace-gas source attribution using a field-

- deployed dual frequency comb spectrometer," *Optica* **5**(4), 320 (2018).
15. G. Ycas, F. R. Giorgetta, K. C. Cossel, et al., "Mid-infrared dual-comb spectroscopy of volatile organic compounds across long open-air paths," *Optica* **6**(2), 165 (2019).
 16. F. R. Giorgetta, J. Peischl, D. I. Herman, et al., "Open-Path Dual-Comb Spectroscopy for Multispecies Trace Gas Detection in the 4.5–5 μm Spectral Region," *Laser & Photonics Reviews* **15**(9), 2000583 (2021).
 17. X. Wu, J. Cui, R. Tong, et al., "Research on Methane Measurement and Interference Factors in Coal Mines," *Sensors* **22**(15), 5608 (2022).
 18. Y. Wang, J. Tang, F. Li, et al., "Measurement of methane emissions from CNG fueling stations in East China," *Environ Sci Pollut Res* **29**(47), 71949–71957 (2022).
 19. T. Xia, S. G. Borjigin, J. Raneses, et al., "Mobile Measurements of Atmospheric Methane at Eight Large Landfills: An Assessment of Temporal and Spatial Variability," *Atmosphere* **14**(6), 906 (2023).
 20. C. Song, J.-J. Zhu, J. L. Willis, et al., "Methane Emissions from Municipal Wastewater Collection and Treatment Systems," *Environ. Sci. Technol.* **57**(6), 2248–2261 (2023).
 21. M. B. Frish, R. T. Wainner, B. D. Green, et al., "Standoff gas leak detectors based on tunable diode laser absorption spectroscopy," in A. A. Belyanin, R. A. Drezek, and C. F. Gmachl, eds. (2005), p. 60100D.
 22. H. Chen, J. Winderlich, C. Gerbig, et al., "High-accuracy continuous airborne measurements of greenhouse gases (CO_2 and CH_4) using the cavity ring-down spectroscopy (CRDS) technique," *Atmos. Meas. Tech.* **3**(2), 375–386 (2010).
 23. C.-H. Lin, R. H. Grant, A. J. Heber, et al., "Application of open-path Fourier transform infrared spectroscopy (OP-FTIR) to measure greenhouse gas concentrations from agricultural fields," *Atmos. Meas. Tech.* **12**(6), 3403–3415 (2019).
 24. S. Lin, J. Chang, J. Sun, et al., "Improvement of the Detection Sensitivity for Tunable Diode Laser Absorption Spectroscopy: A Review," *Front. Phys.* **10**, 853966 (2022).
 25. L. C. Sinclair, I. Coddington, W. C. Swann, et al., "Operation of an optically coherent frequency comb outside the metrology lab," *Opt. Express* **22**(6), 6996 (2014).
 26. C. Gu, Z. Zuo, D. Luo, et al., "Passive coherent dual-comb spectroscopy based on optical-optical modulation with free running lasers," *PhotonIX* **1**(1), 7 (2020).
 27. Z. Zuo, C. Gu, D. Peng, et al., "Broadband mid-infrared molecular spectroscopy based on passive coherent optical–optical modulated frequency combs," *Photon. Res.* **9**(7), 1358 (2021).
 28. H. Cheng, Z. Zhang, X. Hu, et al., "Low noise operation of an all polarization-maintaining figure-9 Er:fiber laser with near-zero cavity dispersion," *Optical Fiber Technology* **87**, 103892 (2024).
 29. J. Dong, M. Pan, Y. Zeng, et al., "Study on the pump reduction of all-polarization-maintaining fiber figure-9 ultrafast laser through active method," *J. Lightwave Technol.* 1–7 (2025).
 30. X. Li, D. Luo, Y. Di, et al., "High-efficiency mid-infrared CW-seeded optical parametric generation in PPLN waveguide," *Opt. Express* **32**(21), 37193 (2024).
 31. D. J. Miller, K. Sun, L. Tao, et al., "Ammonia and methane dairy emission plumes in the San Joaquin Valley of California from individual feedlot to regional scales," *JGR Atmospheres* **120**(18), 9718–9738 (2015).
 32. I. H. Malitson, "Interspecimen Comparison of the Refractive Index of Fused Silica*,†," *J. Opt. Soc. Am.* **55**(10), 1205 (1965).
 33. B. Deng, Y. Shi, and F. Yuan, "Investigation on the structural origin of low thermal expansion coefficient of fused silica," *Materialia* **12**, 100752 (2020).

34. I. E. Gordon, L. S. Rothman, R. J. Hargreaves, et al., "The HITRAN2020 molecular spectroscopic database," *Journal of Quantitative Spectroscopy and Radiative Transfer* **277**, 107949 (2022).
35. O. Kara, F. Sweeney, M. Rutkauskas, et al., "Open-path multi-species remote sensing with a broadband optical parametric oscillator," *Opt. Express* **27**(15), 21358 (2019).
36. K. Sun, L. Tao, D. J. Miller, et al., "Vehicle Emissions as an Important Urban Ammonia Source in the United States and China," *Environ. Sci. Technol.* **51**(4), 2472–2481 (2017).